RESEARCH ARTICLE | MARCH 11 2026

Advanced graphene–MXene–black phosphorus multilayered metasurface sensor for high-sensitivity terahertz brain tumor detection

Jacob Wekalao ; Hussein A. Elsayed; Haifa A. Alqhtani; Abdulkarem H. M. Almawgani; Hussein S. Gumaih; Yousif S. Adam; Ahmed Mehaney ; William Ochen

AIP Advances 16, 035124 (2026)
https://doi.org/10.1063/5.0305214

Advanced graphene–MXene–black phosphorus multilayered metasurface sensor for high-sensitivity terahertz brain tumor detection

Cite as: AIP Advances 16, 035124 (2026); doi: 10.1063/5.0305214
Submitted: 4 October 2025 • Accepted: 8 December 2025 •
Published Online: 11 March 2026

Jacob Wekalao,[1,2,a] Hussein A. Elsayed,[3] Haifa A. Alqhtani,[4] Abdulkarem H. M. Almawgani,[5] Hussein S. Gumaih,[6] Yousif S. Adam,[6] Ahmed Mehaney,[3] and William Ochen[7,b]

AFFILIATIONS

[1] School of Engineering and Technology, National Forensic Sciences University, Gandhinagar 382007, Gujarat, India
[2] Department of Optics and Optical Engineering, University of Science and Technology of China, Hefei 230026, China
[3] Photonic and Phononic Crystals Lab., Physics Department, Faculty of Science, Beni-Suef University, Beni-Suef 62512, Egypt
[4] Department of Biology, College of Science, Princess Nourah bint Abdulrahman University, P.O. Box 84428, Riyadh 11671, Saudi Arabia
[5] Department of Electrical Engineering, College of Engineering, Najran University, Najran, Saudi Arabia
[6] Biological Department, College of Science and Arts, Najran University, Najran, Saudi Arabia
[7] Department of Physics, Kyambogo University, P.O. Box, 1, Kampala, Uganda

[a] jacob1902@mail.ustc.edu.cn and jacob.phdfs2303@nfsu.ac.in
[b] **Author to whom correspondence should be addressed:** wocen@kyu.ac.ug

ABSTRACT

In this research, we present a multilayer metasurface sensor design integrating graphene, MXene, black phosphorus, and gold for the ultra-sensitive detection of brain tumor biomarkers in liquid biopsy samples. The hierarchical structure consists of a MXene-coated rectangular resonator, a black phosphorus-coated square resonator, a gold-coated circular ring, and a graphene-based circular substrate. This architecture was systematically optimized through comprehensive numerical simulations using COMSOL Multiphysics 6.3, integrated with machine learning frameworks. The proposed sensor demonstrates an outstanding sensitivity of 2308 GHz/RIU across a physiologically relevant refractive index range (1.3333–1.4833), significantly outperforming current state-of-the-art devices. Performance analysis identifies an optimal sensing regime at RI = 1.3425, achieving a figure of merit of 20.79 RIU^{-1} and a detection limit as low as 0.079 RIU. Detailed investigations of the transmission spectra under varying graphene chemical potentials (0.1–0.9 eV), incident angles (0°–80°), and geometric modifications of the resonators reveal highly tunable sensing behavior. Furthermore, Random Forest Regression models achieve predictive accuracies of 85%–100%, enabling reliable estimation of sensor performance across diverse operating conditions. Collectively, these results establish a solid foundation for employing advanced 2D material–based metasurfaces in minimally invasive and early-stage brain tumor diagnostics, thereby advancing the capabilities of next-generation liquid biopsy technologies.

I. INTRODUCTION

Malignant neoplasms of the central nervous system represent a formidable clinical challenge in contemporary oncology, with glioblastoma multiforme (GBM) demonstrating particularly aggressive biological behavior and correlating with unfavorable prognostic outcomes despite therapeutic advances in standard-of-care multimodal treatment regimens.[1] Epidemiological data indicate a rising global incidence of primary malignant brain tumors, with ~308 000 newly diagnosed cases documented annually, concomitant with elevated mortality rates and substantial deterioration in patients' health-related quality of life.[2] Early and accurate diagnostic identification constitutes a critical determinant of therapeutic efficacy and clinical outcomes; however, contemporary diagnostic

methodologies frequently detect these neoplastic lesions only upon progression to advanced stages, when therapeutic interventions demonstrate diminished effectiveness.[3]

The molecular architecture of cerebral neoplasms exhibits considerable complexity and temporal heterogeneity, undergoing continuous evolution throughout tumorigenesis and in response to therapeutic selective pressures.[4] Critical protein biomarkers, including glial fibrillary acidic protein (GFAP), S100 calcium-binding protein B (S100B), neuron-specific enolase (NSE), and various tumor-associated antigens, demonstrate aberrant expression profiles that may function as diagnostic indicators.[5] Moreover, the tumor microenvironment manifests distinctive metabolic perturbations, dysregulated growth factor signaling cascades, and immunomodulatory protein expression, collectively generating unique molecular signatures that enable differentiation between neoplastic and normal cerebral parenchyma.[6] Contemporary proteomic investigations have successfully identified numerous brain tumor-associated proteins in both tissue specimens and circulating biological fluids.[7]

Contemporary diagnostic paradigms for cerebral neoplasms predominantly utilize neuroimaging modalities, including contrast-enhanced magnetic resonance imaging (MRI), magnetic resonance spectroscopy (MRS), and positron emission tomography (PET).[8] While these imaging techniques provide essential anatomical and functional data, they demonstrate inherent limitations in detecting microscopic tumor foci, achieving precise delineation of neoplastic margins, and discriminating between therapy-induced changes and authentic tumor recurrence.[9] Specifically, conventional anatomical MRI demonstrates superior performance in structural characterization but exhibits suboptimal specificity for neoplastic tissue identification and encounters difficulties in detecting non-enhancing tumors or differentiating tumor recurrence from treatment-related effects.[10] Advanced MRI methodologies, encompassing perfusion-weighted imaging (PWI), diffusion-weighted imaging (DWI), and MRS, contribute supplementary molecular and physiological information; however, these techniques remain constrained by factors including dependency on magnetic field homogeneity, restricted spatial resolution, and inter-observer variability in diagnostic threshold determination.[11] PET imaging utilizing radiolabeled amino acid tracers enhances tumor visualization and metabolic profiling, thereby facilitating biopsy guidance and therapeutic planning; nevertheless, this modality may be confounded by inflammatory processes or elevated background uptake in cortical gray matter.[12,13]

While conventional tissue biopsy persists as the diagnostic gold standard—providing definitive histopathological confirmation and comprehensive molecular characterization—this invasive procedure carries inherent procedural risks, particularly when targeting deep-seated lesions or eloquent cortical regions.[14] Stereotactic needle biopsy represents the most frequently employed approach, demonstrating high diagnostic yield and comparatively low complication rates; however, the invasive nature of the procedure and potential for neurological deterioration may preclude its utilization in certain clinical scenarios.[15] Notably, radiological diagnoses, particularly for primary central nervous system lymphoma (PCNSL), exhibit substantial concordance with histopathological findings, thereby substantiating the role of tissue biopsy in directing targeted therapeutic strategies and precision medicine applications.[16,17]

Recent technological innovations in biosensor development have established novel paradigms for ultrasensitive biomolecular detection with direct applicability to brain tumor diagnostics.[18–20] Electrochemical impedance spectroscopy (EIS)-based sensors facilitate the detection of molecular binding events through quantification of alterations in electrical impedance, thereby enabling high-sensitivity measurements with rapid temporal response characteristics.[21,22] Surface plasmon resonance (SPR) biosensors leverage the distinctive optical properties of metallic nanostructures to monitor biomolecular interactions in a label-free configuration, consequently enhancing detection specificity.[22,23] Field-effect transistor (FET) biosensors, particularly those incorporating two-dimensional nanomaterials, such as graphene and transition metal dichalcogenides, demonstrate exceptional charge carrier sensitivity, facilitating protein detection at femtomolar concentration ranges.[24] These biosensor platforms collectively exhibit advantageous characteristics, including minimal sample preparation requirements, potential for device miniaturization, and compatibility with microfluidic system integration, thereby positioning them as promising candidates for point-of-care diagnostic applications and early-stage brain tumor detection.[25]

The contemporary period has witnessed substantial advancements in biosensing technology. Sharma *et al.* developed a prism-based hybrid plasmonic waveguide sensor achieving a propagation length of 0.13 cm, ultra-narrow full width at half maximum (FWHM), and a exceptional spectral sensitivity of 29 480 nm/RIU at 0.6328 μm utilizing Ag/Au configuration.[26] Hsu *et al.* proposed an innovative SPR biosensor employing a SiO_2 prism coupled with Ag, SiC, and two-dimensional ZrN layers, demonstrating angular sensitivities reaching 362.45°/RIU for various bacterial targets, characterized by minimal reflectance and pronounced electric field enhancement at the ZrN interface.[27] Sharma *et al.* engineered a gold-coated photonic crystal fiber SPR sensor featuring a quasi-honeycomb architecture operating within the near-infrared spectrum (700–2500 nm), achieving sensitivity exceeding 92% and specificity surpassing 90% for DHOL biomarker detection, with deep neural network (DNN) implementation reducing the computational simulation time by 99.99%.[28] Khan *et al.* demonstrated graphene-based SPR sensing at a four-level dielectric interface, attaining tunable surface plasmon polariton (SPP) sensitivity ranging from 250 to 700°/RIU.[29] Xiao *et al.*[30] developed a polarization-insensitive graphene-based electromagnetically induced transparency (EIT) sensor utilizing orthogonal T-shaped resonator geometry, achieving high sensitivity (>4960 nm/RIU), tunable mid-infrared operational capacity, and substantial potential for biomolecular detection applications. Yuan *et al.* engineered a graphene-based terahertz biosensor for isoquercitrin quantification, demonstrating 500 GHz/RIU sensitivity and high analytical accuracy through one-dimensional convolutional neural network (1D-CNN) modeling, with pronounced potential for real-time, label-free biomedical diagnostic applications.[31] Vaijayanthimala *et al.* designed a high-precision one-dimensional photonic crystal biosensor incorporating MgO and SiO_2 layers, achieving 815 nm/RIU sensitivity and a figure of merit (FOM) of 3369.18 for detecting pathological blood constituents with exceptional accuracy and minimal detection limits.[32] Mahalaksmi *et al.* proposed a one-dimensional photonic crystal biosensor optimized through metaheuristic algorithmic approaches, achieving 842 nm/RIU sensitivity for quantifying glucose concentrations in blood and urine specimens utilizing MgF_2,

BK7, and LiI materials operating within the near-infrared spectral range.[33] Additional comparable investigations are documented in Refs. 6–9.

This investigation delineates a multimodal biosensing platform incorporating a hierarchical nanostructured architecture for the ultrasensitive detection of brain tumor biomarkers and associated protein analytes. The proposed system integrates a resonant graphene-based metasurface with gold (Au) and silver (Ag) nanostructural elements to substantially augment sensitivity, selectivity, and comprehensive sensing performance metrics. The synergistic electromagnetic coupling between these plasmonic materials and graphene's exceptional electron mobility facilitates pronounced electromagnetic field confinement and sharp resonance frequency shifts,[34–37] thereby enabling reliable biomolecular detection at trace concentration levels. To further optimize performance characteristics, machine learning algorithms are implemented to model, predict, and systematically optimize the sensor's spectral response under diverse operational parameters. The design methodology and computational simulations are executed within the terahertz (THz) frequency domain, where biomolecular interactions manifest distinctive spectral signatures. Collectively, this analytical framework demonstrates the translational potential of synergistically combining hybrid nanomaterial architectures with artificial intelligence-driven optimization strategies to advance next-generation biosensing technologies for clinical diagnostics.

II. MATERIALS AND METHODS

The sensor uses a set of nested resonators arranged in a hierarchical layout to improve refractive index detection. The central element is a rectangular structure measuring 4 μm by 1 μm that is coated with MXene, a transition metal carbide or nitride material with high electrical conductivity and strong interaction with terahertz fields. This MXene-coated element is placed on a 3 μm by 3 μm square platform coated with black phosphorus. The material has high carrier mobility and directional anisotropy, which supports tunable terahertz response. An annular ring surrounds these inner components. The ring has an inner diameter of 4.5 μm and an outer diameter of 5 μm. A gold coating on the ring produces plasmonic field enhancement by exciting surface plasmons and concentrating energy near the inner resonators. The full structure is supported by a circular substrate with a radius of 7 μm that carries a single layer of graphene about 0.34 nm thick. Graphene provides electronic and optical tunability that influences plasmon behavior as the refractive index of the surrounding analyte changes. This layered resonator layout improves field confinement, strengthens electromagnetic coupling, and supports high Q-factor

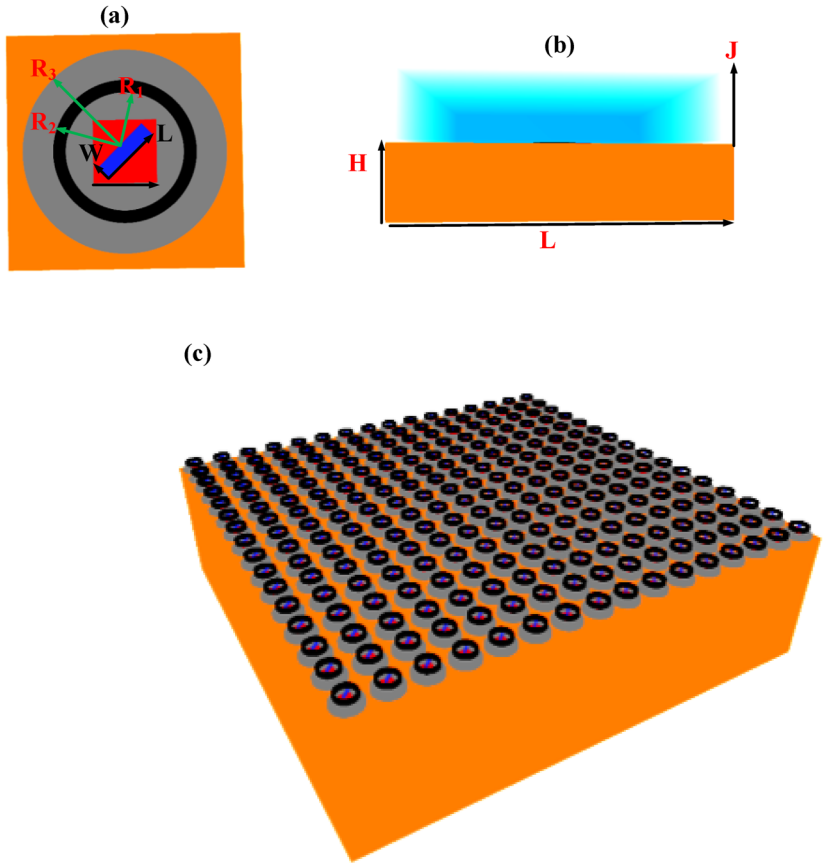

FIG. 1. Structural layout of the nested terahertz metasurface sensor showing the rectangular MXene element, black phosphorus platform, gold-coated ring, and graphene substrate in top, cross-sectional, and 3D views.

modes, which together increase detection sensitivity and selectivity. Figures 1(a)–1(c) show the top, cross-sectional, and three-dimensional views of the geometry and material arrangement.

Real-time fabrication of the sensor follows a sequential microfabrication workflow. A silicon or quartz wafer is first cleaned and prepared as the base. A thin graphene layer is transferred onto the substrate using a wet or dry transfer process. Electron beam lithography defines the circular base pattern, followed by metal deposition and lift-off to form the gold ring. A second lithography step patterns the 3 μm by 3 μm square region, and black phosphorus is mechanically exfoliated or deposited under inert conditions to prevent degradation. The central rectangular region is then patterned, after which MXene flakes or films are deposited through spin coating or vacuum filtration and aligned to achieve uniform coverage. Each layer is inspected using optical microscopy and atomic force microscopy to confirm thickness and alignment before the next step. The completed device is released from the fabrication chamber and sealed in a controlled environment for real-time terahertz testing.

Unlike previous studies that predominantly focused on single-layer graphene absorbers or isolated MXene-based resonators, our approach leverages a multilayered graphene–MXene–black phosphorus architecture that enables hybrid plasmonic–anisotropic coupling. Prior reports typically achieved sensitivities in the range of 0.2–0.5 THz/RIU with limited electrical tunability; however, by integrating multiple 2D materials, our sensor exhibits markedly enhanced field confinement and broadband tunability. A comparative analysis of recent state-of-the-art sensor designs mentioned in the Introduction shows that existing designs often suffer from weak interlayer coupling, modest resonance quality, or a lack of machine-learning-driven optimization. These trends underscore the novelty of our proposed structure, which not only surpasses earlier sensitivities but also introduces an interpretable and data-driven optimization strategy that has not been previously demonstrated.

A. Electromagnetic formulation for plasmonic resonators

First, we begin with the time-harmonic representation of Maxwell's curl equations under the assumption of monochromatic excitation with angular frequency ω, yielding the coupled first-order partial differential operators acting upon the phasor representations of electromagnetic fields,

$$\nabla \times \mathbf{E}(\mathbf{r},\omega) = i\omega\mu_0\mu_r(\mathbf{r})\mathbf{H}(\mathbf{r},\omega), \tag{1}$$

$$\nabla \times \mathbf{H}(\mathbf{r},\omega) = -i\omega\varepsilon_0\varepsilon_r(\mathbf{r},\omega)\mathbf{E}(\mathbf{r},\omega) + \mathbf{J}_s(\mathbf{r},\omega), \tag{2}$$

wherein $\mathbf{E}(\mathbf{r},\omega)$ and $\mathbf{H}(\mathbf{r},\omega)$ denote the complex-valued electric and magnetic field phasors, respectively, $\mu_r(\mathbf{r})$ represents the spatially dependent relative permeability tensor (generally unity for non-magnetic plasmonic systems), $\varepsilon_r(\mathbf{r},\omega)$ encapsulates the frequency-dispersive and potentially anisotropic relative permittivity distribution, and $\mathbf{J}_s(\mathbf{r},\omega)$ embodies impressed surface current densities arising from external excitation or two-dimensional conductive sheets.

B. Constitutive relations and material response kernels

1. Bulk anisotropic dielectric: Black phosphorus

For orthorhombic layered materials, such as black phosphorus exhibiting crystallographic anisotropy, a diagonal permittivity tensor aligned with the principal crystallographic axes is invoked,

$$\boldsymbol{\varepsilon}_{\mathrm{BP}}(\omega) = \varepsilon_0\begin{pmatrix}\varepsilon_x(\omega) & 0 & 0\\ 0 & \varepsilon_y(\omega) & 0\\ 0 & 0 & \varepsilon_z(\omega)\end{pmatrix}, \tag{3}$$

where each diagonal component $\varepsilon_\alpha(\omega)$ $(\alpha \in \{x,y,z\})$ may itself incorporate Lorentzian oscillators modeling interband transitions,

$$\varepsilon_\alpha(\omega) = \varepsilon_{\alpha,\infty} + \sum_{j=1}^{N_\alpha} \frac{f_{\alpha,j}\omega_{p,\alpha}^2}{\omega_{\alpha,j}^2 - \omega^2 - i\gamma_{\alpha,j}\omega}. \tag{4}$$

2. Dispersive metallic response: Drude–Lorentz model

Noble metals (Au, Ag) and doped semiconductors exhibit free-carrier response captured by the Drude formalism superimposed upon a high-frequency background polarizability,

$$\varepsilon_{\mathrm{m}}(\omega) = \varepsilon_\infty - \frac{\omega_{\mathrm{p}}^2}{\omega^2 + i\gamma\omega} + \sum_{k=1}^{M} \frac{\Delta\varepsilon_k\Omega_k^2}{\Omega_k^2 - \omega^2 - i\Gamma_k\omega}. \tag{5}$$

Here, ω_{p} denotes the bulk plasmon frequency, γ denotes the electron collision rate, ε_∞ accounts for core-electron polarizability, and the summation captures interband critical-point contributions with oscillator strengths $\Delta\varepsilon_k$, resonance frequencies Ω_k, and damping rates Γ_k.

3. Two-dimensional conductive sheets: Graphene and MXene

Graphene and transition-metal carbides/nitrides (MXenes) are modeled as infinitesimally thin conductive interfaces characterized by frequency-dependent surface conductivities $\sigma_{\mathrm{g}}(\omega)$ and $\sigma_{\mathrm{M}}(\omega)$, respectively. For intrinsic or doped graphene within the random-phase approximation, the Kubo formula decomposed into intraband (Drude-like) and interband contributions is invoked,

$$\sigma_{\mathrm{g}}(\omega,\mu_{\mathrm{c}},T) = \sigma_{\mathrm{intra}}(\omega,\mu_{\mathrm{c}},T) + \sigma_{\mathrm{inter}}(\omega,\mu_{\mathrm{c}},T), \tag{6}$$

$$\sigma_{\mathrm{intra}}(\omega,\mu_{\mathrm{c}},T) = \frac{2e^2k_{\mathrm{B}}T}{\pi\hbar^2}\frac{i}{\omega + i\tau^{-1}}\ln\left[2\cosh\left(\frac{\mu_{\mathrm{c}}}{2k_{\mathrm{B}}T}\right)\right], \tag{7}$$

$$\sigma_{\mathrm{inter}}(\omega,\mu_{\mathrm{c}},T) = \frac{e^2}{4\hbar}\left[G\left(\frac{\hbar\omega}{2}\right) + i\frac{4\hbar\omega}{\pi}\int_0^\infty \frac{G(\xi) - G(\hbar\omega/2)}{(\hbar\omega)^2 - 4\xi^2}d\xi\right], \tag{8}$$

with $G(\xi) = \sinh(\xi/k_{\mathrm{B}}T)/[\cosh(\mu_{\mathrm{c}}/k_{\mathrm{B}}T) + \cosh(\xi/k_{\mathrm{B}}T)]$, μ_{c} being the chemical potential, T being the temperature, and τ being the momentum relaxation time. For MXene, a phenomenological Drude–Smith or generalized Drude form incorporating backscattering is adopted,

$$\sigma_{\mathrm{M}}(\omega) = \frac{\sigma_{\mathrm{DC}}}{1 - i\omega\tau_{\mathrm{M}}}\left[1 + \frac{c_1}{1 - i\omega\tau_{\mathrm{M}}}\right], \tag{9}$$

where $c_1 \in [-1, 0]$ quantifies carrier localization.

C. Electromagnetic boundary conditions at 2D material interfaces

At a planar interface $\mathcal{S}$ (parameterized by $\mathbf{r}_\parallel$) supporting a conductive sheet with surface conductivity $\sigma(\omega)$, the tangential magnetic field experiences a discontinuity governed by the induced surface current density,

$$\hat{\mathbf{n}} \times \left[\mathbf{H}_2(\mathbf{r}_\parallel, \omega) - \mathbf{H}_1(\mathbf{r}_\parallel, \omega)\right] = \mathbf{J}_{\mathrm{s}}(\mathbf{r}_\parallel, \omega) = \sigma(\omega)\mathbf{E}_\parallel(\mathbf{r}_\parallel, \omega), \tag{10}$$

where $\hat{\mathbf{n}}$ is the unit normal to $\mathcal{S}$, subscripts 1, 2 denote fields immediately below and above the interface, and $\mathbf{E}_\parallel$ is the tangential electric field (assumed continuous). This sheet-conductivity boundary condition couples the electromagnetic fields across the 2D material and must be incorporated into the weak-form variational statement or finite-difference stencil.

D. Eigenvalue formulation via vector wave equation

Eliminate the magnetic field phasor from the coupled curl equations by applying the curl operator to Faraday's law and substituting Ampère's law, yielding the second-order vector Helmholtz equation for the electric field,[38,39]

$$\nabla \times \left[\mu_r^{-1}(\mathbf{r})\nabla \times \mathbf{E}(\mathbf{r}, \omega)\right] - k_0^2 \varepsilon_r(\mathbf{r}, \omega)\mathbf{E}(\mathbf{r}, \omega) = i\omega\mu_0 \mathbf{J}_{\mathrm{s}}(\mathbf{r}, \omega) \tag{11}$$

with $k_0 = \omega/c$ being the free-space wavenumber. For source-free resonator configurations ($\mathbf{J}_{\mathrm{s}} = \mathbf{0}$), this reduces to a generalized eigenvalue problem,[40–42]

$$\mathcal{L}[\mathbf{E}_n] \equiv \nabla \times \left[\mu_r^{-1}\nabla \times \mathbf{E}_n(\mathbf{r})\right] = k_{0,n}^2 \varepsilon_r(\mathbf{r}, \omega_n)\mathbf{E}_n(\mathbf{r}). \tag{12}$$

Solve for the discrete spectrum of complex eigenfrequencies $\tilde{\omega}_n = \omega_n - i\kappa_n$ (where ω_n is the resonance center frequency and κ_n is the damping rate) and corresponding modal fields $\mathbf{E}_n(\mathbf{r})$ subject to appropriate radiation or perfectly matched-layer boundary conditions. The intrinsic quality factor follows from

$$Q_n = \frac{\omega_n}{2\kappa_n} = \frac{\mathrm{Re}(\tilde{\omega}_n)}{2\,\mathrm{Im}(\tilde{\omega}_n)}. \tag{13}$$

Numerical solution typically employs the finite-element method (FEM) with edge elements (Nédélec spaces) or finite-difference frequency-domain (FDFD) discretization on Yee grids, accompanied by iterative eigensolvers (Arnoldi, Jacobi–Davidson) for large-sparse non-Hermitian matrices.

E. Quasi-static dispersion relation for localized surface plasmon polaritons

In the electrostatic approximation valid for $\lambda \gg$ lateral feature size, surface plasmon polaritons (SPPs) at a 2D conductor sandwiched between dielectrics ε_1 and ε_2 obey a simplified dispersion,[43–45]

$$q_{\mathrm{SPP}}(\omega) \approx \frac{i\omega\varepsilon_0(\varepsilon_1(\omega) + \varepsilon_2(\omega))}{\sigma(\omega)}, \tag{14}$$

where q_{SPP} is the complex in-plane wavevector. Inversion yields the resonance condition,

$$\sigma(\omega_{\mathrm{res}}) = i\omega_{\mathrm{res}}\varepsilon_0 \frac{\varepsilon_1(\omega_{\mathrm{res}}) + \varepsilon_2(\omega_{\mathrm{res}})}{q_{\mathrm{SPP}}}. \tag{15}$$

Losses enter through $\mathrm{Im}[\sigma(\omega)] > 0$ (intraband scattering) and $\mathrm{Im}[\varepsilon_{1,2}] > 0$ (substrate absorption), leading to a finite $\mathrm{Im}[q_{\mathrm{SPP}}]$ and hence damped propagation. For graphene with Drude intraband conductivity, explicit substitution gives[46,47]

$$q_{\mathrm{SPP}}(\omega) \approx -i\frac{\pi\hbar^2(\varepsilon_1 + \varepsilon_2)\left(\omega + i\tau^{-1}\right)}{e^2\mu_{\mathrm{c}}}\omega. \tag{16}$$

F. First-order perturbation theory for analyte-induced resonance shifts

Consider a weak refractive-index perturbation $\Delta n(\mathbf{r})$ localized in volume V_{a} (the analyte region), corresponding to a permittivity change $\Delta\varepsilon(\mathbf{r}) = 2n_0\Delta n(\mathbf{r})$, where n_0 is the background index. The fractional shift in eigenfrequency is, to first order in $\Delta\varepsilon$,

$$\frac{\Delta\omega_n}{\omega_{n,0}} = -\frac{1}{2}\frac{\int_{V_{\mathrm{a}}} \Delta\varepsilon(\mathbf{r})\ |\mathbf{E}_{n,0}(\mathbf{r})|^2 dV}{\int_{V_{\mathrm{tot}}} \varepsilon(\mathbf{r})\ |\mathbf{E}_{n,0}(\mathbf{r})|^2 dV}. \tag{17}$$

Here, $\mathbf{E}_{n,0}$ is the unperturbed modal field (normalized such that the denominator equals the stored electric energy), and the negative sign reflects that increased permittivity redshifts the resonance. Define the bulk refractive-index sensitivity,

$$S_n \equiv \frac{\partial f_{\mathrm{res}}}{\partial n} = -\frac{f_{n,0}}{2n_0}\frac{\int_{V_{\mathrm{a}}} |\mathbf{E}_{n,0}|^2 dV}{\int_{V_{\mathrm{tot}}} \varepsilon|\mathbf{E}_{n,0}|^2 dV}\,[\mathrm{Hz\ per\ RIU}], \tag{18}$$

and the figure of merit,

$$\mathrm{FOM} = \frac{S_n}{\mathrm{FWHM}} = \frac{S_n Q_n}{f_{n,0}} = -\frac{Q_n}{2n_0}\frac{\int_{V_{\mathrm{a}}} |\mathbf{E}_{n,0}|^2 dV}{\int_{V_{\mathrm{tot}}} \varepsilon|\mathbf{E}_{n,0}|^2 dV}, \tag{19}$$

where $\mathrm{FWHM} = f_{n,0}/Q_n$. Maximizing FOM requires simultaneous enhancement of Q_n (minimizing radiation and Ohmic losses) and the concentration of modal energy in V_{a} (field confinement).

G. Local field enhancement and detection figures of merit

Quantify the electromagnetic enhancement at position $\mathbf{r}$ relative to the incident-field amplitude,

$$\mathcal{F}_{\mathrm{E}}(\mathbf{r}, \omega) = \frac{|\mathbf{E}_{\mathrm{total}}(\mathbf{r}, \omega)|}{|\mathbf{E}_{\mathrm{inc}}(\omega)|}. \tag{20}$$

Peak enhancement $\mathcal{F}_{\mathrm{E,\,max}}$ typically occurs at hot-spots near sharp metallic features or at the graphene/metal interface. The detection signal scales with the spatially integrated field intensity weighted by the analyte permittivity,

$$\mathcal{I}_{\mathrm{detect}} \propto \int_{V_{\mathrm{a}}} \varepsilon(\mathbf{r}, \omega)\ |\mathbf{E}(\mathbf{r}, \omega)|^2 dV. \tag{21}$$

Higher $\mathcal{I}_{\mathrm{detect}}$ yields larger measurable shifts $\Delta\omega$ for a given Δn.

H. Power dissipation and scattering: Poynting vector decomposition

Compute the time-averaged power flow via the complex Poynting vector,[48–50]

$$\langle \mathbf{S} \rangle = \frac{1}{2}\mathrm{Re}\left[\mathbf{E}(\mathbf{r},\omega) \times \mathbf{H}^*(\mathbf{r},\omega)\right]. \tag{22}$$

Ohmic dissipation density in a lossy medium follows from

$$p_{\mathrm{loss}}(\mathbf{r},\omega) = \frac{1}{2}\mathrm{Re}\left[\mathbf{J}^* \cdot \mathbf{E}\right] = \frac{1}{2}\omega\varepsilon_0 \,\mathrm{Im}\left[\varepsilon_r(\mathbf{r},\omega)\right] \,|\mathbf{E}(\mathbf{r},\omega)|^2. \tag{23}$$

The total dissipated power and radiated power are obtained by volume/surface integrals,

$$P_{\mathrm{diss}} = \int_{V_{\mathrm{resonator}}} p_{\mathrm{loss}} dV, \quad P_{\mathrm{rad}} = \oint_{S_\infty} \langle \mathbf{S} \rangle \cdot \hat{\mathbf{n}} dS. \tag{24}$$

The quality factor decomposes into radiative and non-radiative channels,

$$\frac{1}{Q_n} = \frac{1}{Q_{\mathrm{rad}}} + \frac{1}{Q_{\mathrm{nr}}} = \frac{P_{\mathrm{rad}}}{\omega_n W} + \frac{P_{\mathrm{diss}}}{\omega_n W}, \tag{25}$$

where $W = \frac{1}{4}\int\left[\varepsilon_0\varepsilon_r|\mathbf{E}|^2 + \mu_0\mu_r|\mathbf{H}|^2\right]dV$ is the stored electromagnetic energy.

I. Spectral line shape and experimental observables

The frequency-domain transmission or reflection coefficient near a resonance exhibits a Lorentzian (or asymmetric Fano) profile,

$$T(\omega) \approx T_{\mathrm{bg}} + \frac{A\Gamma_{\mathrm{rad}}^2}{(\omega - \omega_n)^2 + \kappa_n^2}, \tag{26}$$

with center frequency $\omega_n = \mathrm{Re}(\tilde{\omega}_n)$ and half-width at half-maximum $\kappa_n = \mathrm{Im}(\tilde{\omega}_n) = \omega_n/(2Q_n)$. Measured absorption/scattering spectra directly reveal κ_n, enabling the extraction of Q_n and decomposition into loss channels via auxiliary simulations.

J. Mesh convergence, loss-channel separation, and material parameter sweeps

1. Mesh refinement strategy

Ensure adaptive mesh refinement in regions of high field gradient (near edges, 2D sheets) such that

$$\max_{\mathrm{element}\ \Omega_e}\left(\frac{h_e}{\delta_{\mathrm{skin}}}, \frac{h_e}{\lambda_{\mathrm{SPP}}/n_{\mathrm{mesh}}}\right) < 1, \tag{27}$$

where h_e is the element size, $\delta_{\mathrm{skin}} = \sqrt{2/(\omega\mu_0\sigma)}$ is the skin depth, λ_{SPP} is the SPP wavelength, and $n_{\mathrm{mesh}} \approx 10$ points per wavelength.

2. Radiative vs non-radiative loss partitioning

Compare eigenfrequencies computed with and without radiation boundaries (PML vs PEC) to isolate Q_{rad} and then infer Q_{nr} from the measured total Q_n. This formulation treats anisotropic bulk media, frequency-dispersive metals, and atomically thin conductive sheets within a unified electromagnetic eigenvalue framework. Perturbation theory links analyte-induced permittivity changes to measurable spectral shifts, while Poynting-vector decomposition partitions loss mechanisms. The methodology directly informs finite-element/finite-difference solvers, adaptive meshing protocols, and parametric optimization campaigns for next-generation plasmonic and polaritonic resonators.

3. Clinical validation feasibility

Translating the metasurface sensor to clinical use requires addressing issues such as nonspecific biofouling from proteins and salts in biological fluids. Antifouling coatings and microfluidic filtration can limit unwanted adsorption. Target specificity for glioma biomarkers is established by attaching antibodies or aptamers to the graphene or gold regions. Flexible substrates allow incorporation into portable devices. For measurements in plasma or cerebrospinal fluid, microfluidic cartridges with filtration and reference channels help maintain stable output. Clinical evaluation involves testing patient samples with antibody-functionalized sensors and comparing results with an established assay, such as ELISA. Signal changes arise from shifts in resonance amplitude caused by biomarker-induced refractive index variations. The graphene–MXene interface supports strong plasmonic coupling because MXene has a high free-carrier density that increases capacitive interaction across the van der Waals gap and extends the plasmon propagation length in graphene, which concentrates the electric field near the sensing region. Black phosphorus adds anisotropic plasmon control through its direction-dependent permittivity tensor, which produces asymmetric charge motion, anisotropic field confinement, and mode splitting that improve responsiveness to biological analytes.

III. RESULTS AND DISCUSSION

Numerical modeling was performed using the RF Module of COMSOL Multiphysics 6.3. The device was excited by a linearly polarized plane wave incident perpendicular to the surface along the Z-axis, with the electric field oriented along the X-axis. Perfectly Matched Layers (PMLs) were applied at the simulation boundaries to absorb outgoing waves and prevent artificial reflections. A free tetrahedral meshing approach was employed within the computational domain, with the mesh refined to 0.05–0.1 μm around the resonator edges to preserve numerical accuracy. Frequency-domain simulations were conducted over the 0.2–1.6 THz range, with a spectral resolution of 0.001 THz, and solver convergence thresholds were stringently defined to ensure numerical stability. Validation tests comparing medium and fine mesh configurations revealed discrepancies below 1%, confirming the robustness of the computational results. The analysis primarily focused on evaluating transmission characteristics to optimize sensor performance, with transmission spectra corresponding to different geometric configurations presented in Secs. III A–III C.

The impact of adjusting graphene's chemical potential (GCP) was examined comprehensively across a range of 0.1–0.9 eV with 0.1 eV intervals, as demonstrated in Figs. 2(a) and 2(b). These adjustments yielded substantial modifications in transmission behavior. With rising chemical potential values, transmission consistently decreased from roughly 97.6% down to 45.3%. This phenomenon stems from amplified absorption resulting from

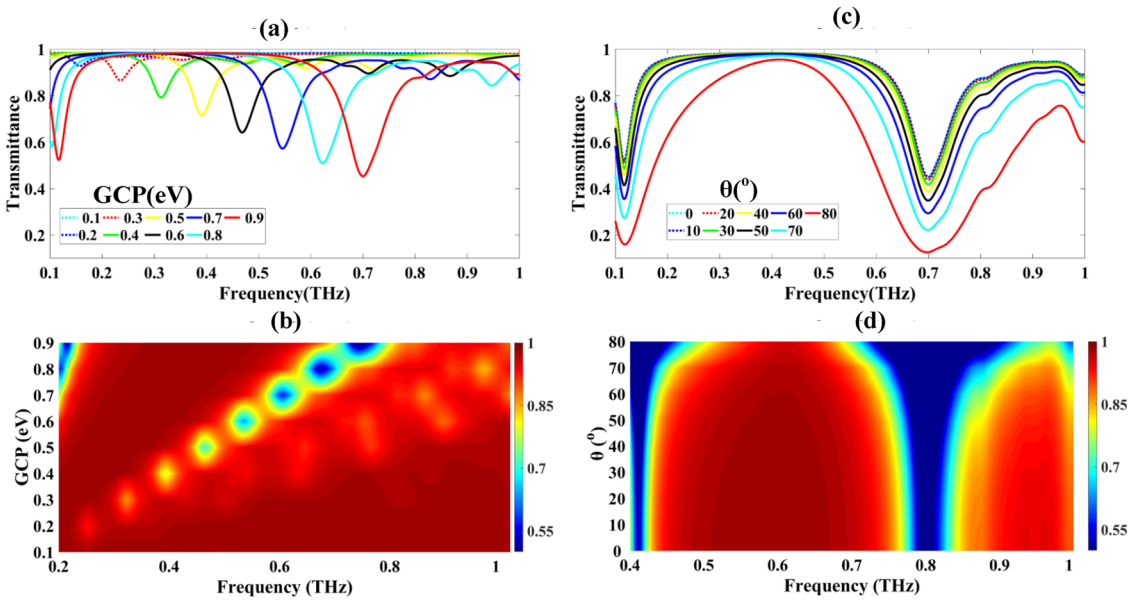

FIG. 2. [(a)–(d)] Transmission spectra showing (a) the effect of varying graphene chemical potential from 0.1 to 0.9 eV, (b) angular dependence of transmission from 0° to 80° incidence, (c) parametric variation of geometric dimensions, and (d) comparative performance under different polarization states.

graphene's adjustable surface conductivity at terahertz frequencies. Such tuning capability demonstrates graphene's remarkable potential for adaptive THz control and detection applications, since the elevated chemical potentials strengthen electromagnetic interaction and consequently enhance sensing performance. The role of incidence angle (AOI) was examined from perpendicular orientation up to 80° using 10° steps, as demonstrated in Figs. 2(c) and 2(d). Findings revealed a nonlinear transmission reduction as AOI increased,

TABLE I. Key simulation parameters and their effects on the transmittance of the graphene-based THz metasurface sensor.

Parameter	Range/values	Observed transmittance/remarks
Graphene chemical potential (GCP, μ_c)	0.1 eV → 0.9 eV (increment 0.1 eV)	Progressive decrease in transmittance with increasing μ_c: 0.1 eV: 97.60% 0.2 eV: 90.22% 0.3 eV: 82.92% 0.4 eV: 74.57% 0.5 eV: 65.43% 0.6 eV: 56.79% 0.7 eV: 50.12% 0.8 eV: 47.89% 0.9 eV: 45.35% trend indicates enhanced absorption due to increased surface conductivity of graphene
Angle of incidence (AOI)	0° → 80° (increment 10°)	Nonlinear reduction in transmittance with increasing AOI: 0°: 45.35% 10°: 44.98% 20°: 43.84% 30°: 41.86% 40°: 38.95% 50°: 34.90% 60°: 29.45% 70°: 22.23% 80°: 12.67% attributed to angular dependence of wave–metasurface interactions and Fresnel transmission effects
Frequency sweep	0.2–1.6 THz (increment 0.001 THz)	Transmission spectrum analyzed to identify resonant features and optimize sensor performance
Mesh resolution	0.05–0.1 μm near resonator edges	Ensured numerical convergence; deviation between medium and fine grids <1%
Solver tolerance	1×10^{-6}	High numerical precision for stable simulation results

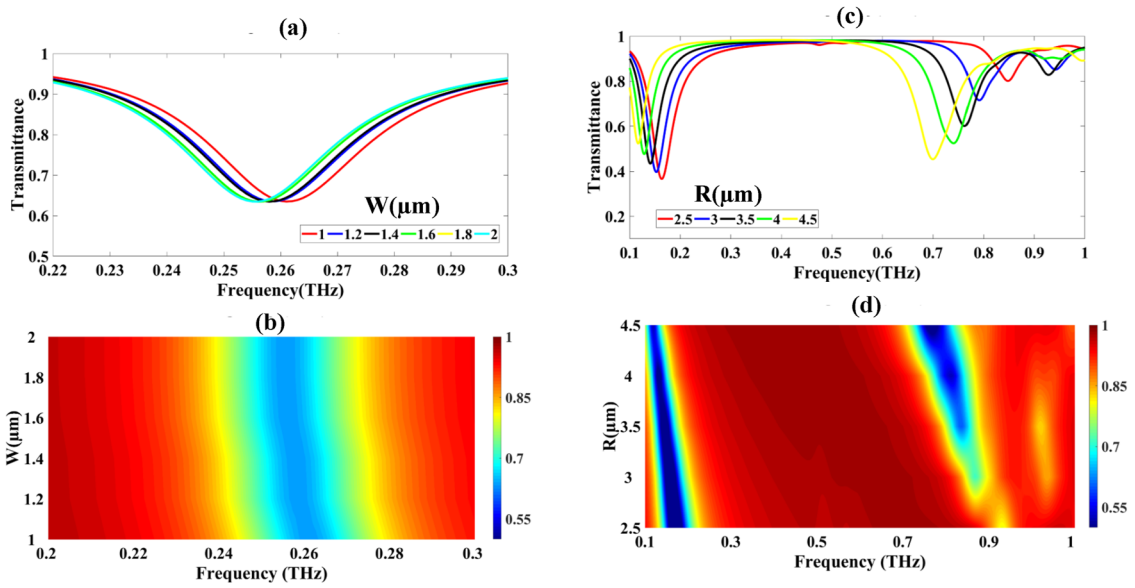

FIG. 3. [(a)–(d)] Transmission characteristics demonstrating [(a) and (b)] minimal sensitivity to rectangular element width variation from 1 to 2 μm with consistent ~62.5% transmittance drops and [(c) and (d)] significant sensitivity to circular ring diameter changes from 2.5 to 4.5 μm, exhibiting transmittance reductions ranging from 36.60% to 47.66%.

with measurements falling progressively from 45.3% to 12.7%. This pattern results from how the angle affects coupling between incoming electromagnetic radiation and the directionally dependent metasurface structure. At steeper angles, both TE and TM polarization components experience altered transmission, resulting in substantial transmittance degradation at oblique incidence.

Table I summarizes the key simulation parameters used to analyze the graphene-based THz metasurface sensor. It details the role of each parameter, including graphene chemical potential, angle of incidence, frequency sweep, mesh resolution, solver tolerance, boundary conditions, and wave polarization. Table I also presents the specific ranges or values considered for each parameter. Finally, it highlights the observed effects of these parameters on the sensor's transmittance and overall performance.

Figures 3(a) and 3(b) illustrate that varying the width of the rectangular resonator component from 1 to 2 μm in 0.2 μm increments results in transmittance reductions of ~62.48%, 62.52%, 62.47%, 62.46%, 62.46%, and 62.47%, respectively. The minimal variation across these values indicates that width adjustments within this range exert an insignificant impact on the resonant behavior of

TABLE II. Comprehensive numerical performance analysis of the proposed brain tumor detection biosensor.

n (RIU)	1.3333	1.3412	1.3425	1.3531	1.3951	1.4121	1.432	1.4412	1.447	1.4591	1.4833
f (THz)	0.318	0.317	0.316	0.315	0.314	0.313	0.312	0.311	0.31	0.309	0.308
df (THz)		0.001	0.001	0.001	0.001	0.001	0.001	0.001	0.001	0.001	0.001
dn (RIU)		0.0079	0.0013	0.0106	0.042	0.017	0.0199	0.0092	0.0058	0.0121	0.0242
S (GHz/RIU)		127	769	94	24	59	50	109	172	83	41
FWHM (THz)	0.324	0.324	0.324	0.324	0.324	0.324	0.324	0.324	0.324	0.324	0.324
FOM (RIU^{-1})		0.391	2.374	0.291	0.073	0.182	0.155	0.335	0.532	0.255	0.128
Q	0.981	0.978	0.975	0.972	0.969	0.966	0.963	0.960	0.957	0.954	0.951
DL		7.240	1.191	9.714	38.489	15.579	18.237	8.431	5.315	11.089	22.177
DR	0.559	0.557	0.555	0.553	0.552	0.550	0.548	0.546	0.545	0.543	0.541
DA	3.086	3.086	3.086	3.086	3.086	3.086	3.086	3.086	3.086	3.086	3.086
SR		0.916	0.916	0.916	0.916	0.916	0.916	0.916	0.916	0.916	0.916
SNR		0.003	0.003	0.003	0.003	0.003	0.003	0.003	0.003	0.003	0.003
X		0.001	0.001	0.001	0.001	0.001	0.001	0.001	0.001	0.001	0.001

the structure. This stability can be attributed to negligible alterations in the effective refractive index, which predominantly governs the resonance mechanism (Table II).

In contrast, as shown in Figs. 3(c) and 3(d), modifying the diameter of the circular ring resonator from 2.5 to 4.5 μm in 0.5 μm increments produces transmittance reductions of 36.60%, 39.70%, 43.40%, 47.66%, and 45.35%, respectively. These results reveal a pronounced dependence of the electromagnetic response on the ring geometry. The enhanced sensitivity arises from intensified field confinement and modal interactions within the circular configuration, both of which strongly influence resonance dynamics. The reduction in mode volume within the ring structure amplifies electromagnetic coupling, thereby accounting for the significant transmittance fluctuations observed.

The investigated refractive index (RI) range of 1.3333–1.4833 was deliberately chosen to emulate biologically relevant fluidic environments, particularly those characteristic of cancer-associated biomarkers and tissue-mimicking aqueous media. This broad RI spectrum allows the metasurface sensor's resonance response to be evaluated under realistic clinical and biochemical conditions. The detection performance corresponding to this range is illustrated in Figs. 4(a) and 4(b). As observed, the metasurface exhibits highly stable and well-defined resonance features. The maximum transmittance values were recorded as 98.201%, 98.153%, 98.145%, 98.079%, 97.809%, 97.696%, 97.560%, 97.496%, 97.456%, 97.371%, and 97.197%, while the corresponding minimum transmittance values were 29.429%, 29.366%, 29.360%, 29.269%, 28.938%, 28.808%, 28.662%, 28.595%, 28.546%, 28.465%, and 28.283%, respectively.

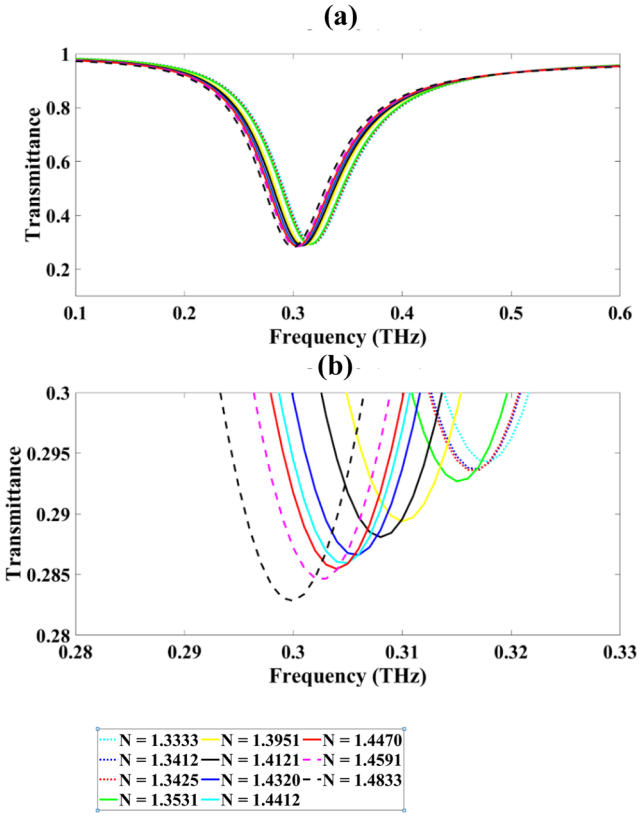

FIG. 4. [(a) and (b)] Resonance frequency shifts under different analyte conditions for brain tumor detection. Progressive redshifts (e.g., from 0.83 to 0.75 THz) indicate stronger analyte interaction and increased refractive index. Figures 6(c) and 6(e) represent high-sensitivity responses due to stronger binding or higher biomarker concentration.

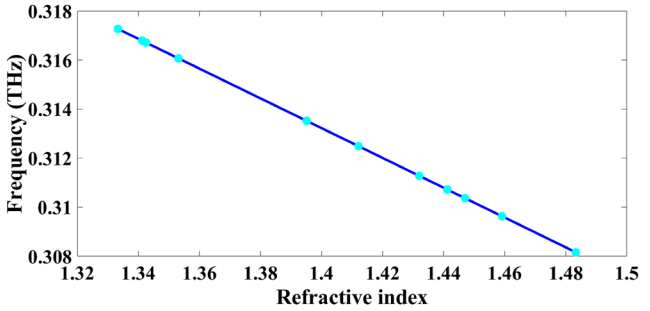

FIG. 5. The correlation between the resonance frequency and refractive index measurements.

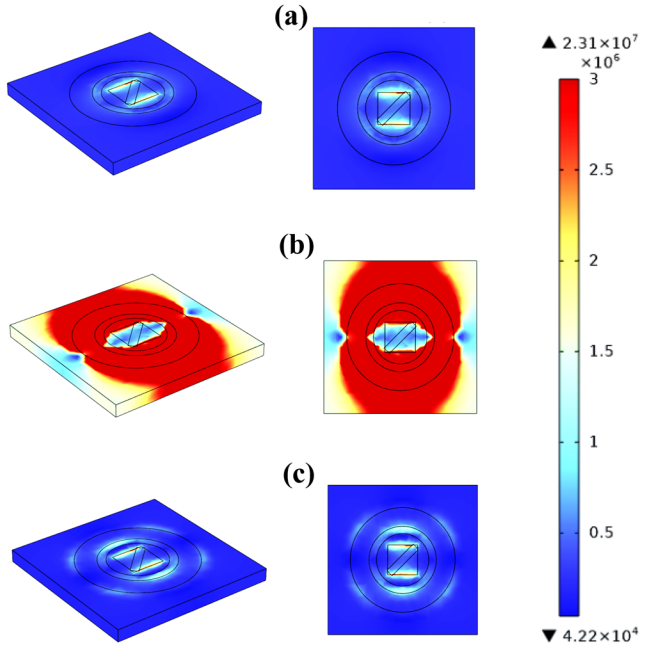

FIG. 6. [(a)–(c)] Normalized electric field distribution (|E|) for RI = 1.3425 at 0.25, 0.325 and 0.4 THz.

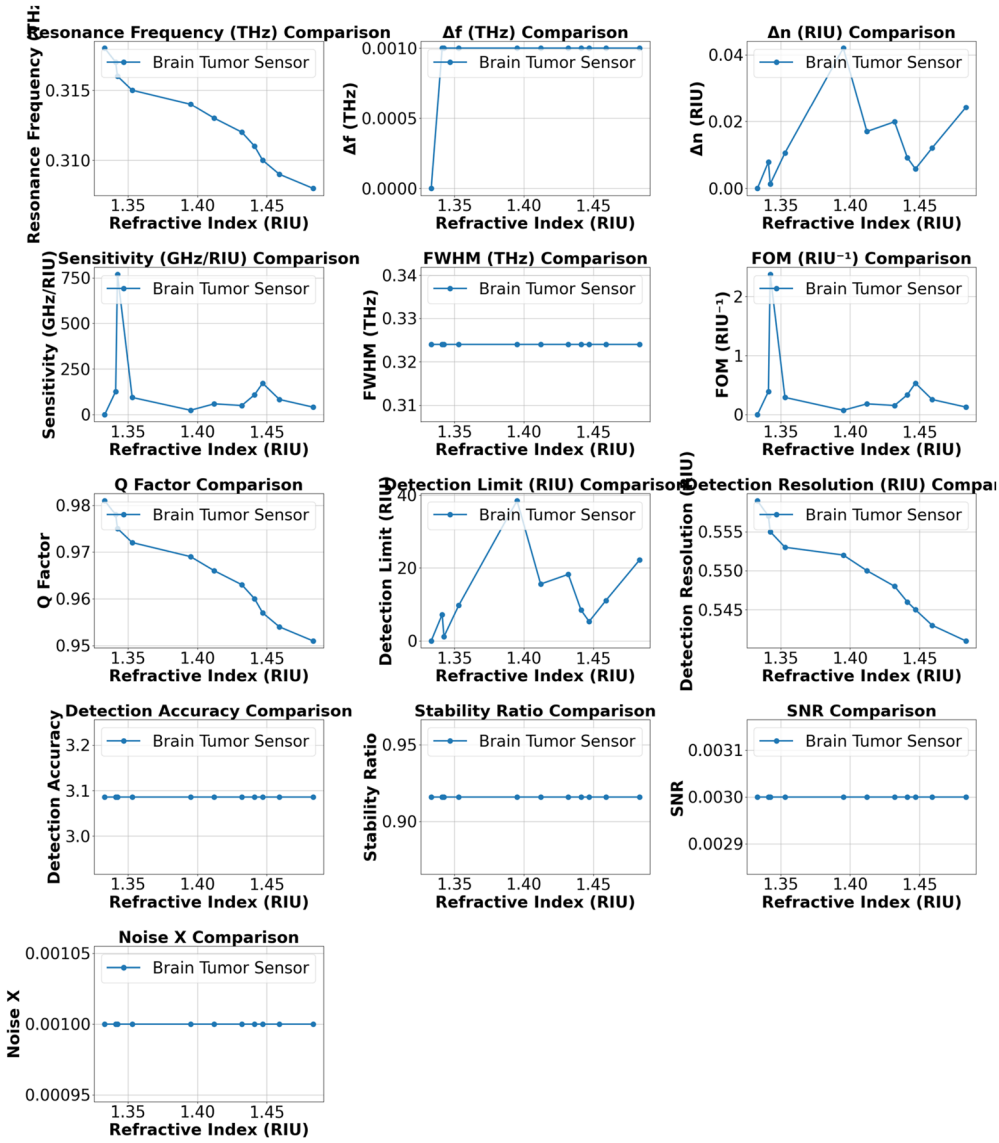

FIG. 7. Comparison of the key performance metrics of the proposed brain tumor detection biosensor across varying refractive indices.

TABLE III. Comparative analysis of the proposed sensor performance against established methodologies.

	RIs	S (GHz/RIU)	Materials	Application
51	1.565–1.754	1000	Au/Ag/graphene	Amino acid detection
52	1.34–1.43	130	Graphene	Hemoglobin
53	1.373–1.402	500	Graphene	Malaria detection
54	1.34–1.43	150	Graphene	Hemoglobin
55	1.334–1.355	800	Graphene, MX, and Bp	Covid 19 detection
56	1–1.07	200	Graphene	Gas detection
Proposed	1.3333–1.4833	769	Mxene/Au/graphene	Brain tumor detection

These pronounced transmission extrema indicate strong resonance dip formation and enhanced field–matter coupling throughout the entire RI sweep. The resonance frequencies corresponding to the transmittance peaks occur at 0.318, 0.317, 0.316, 0.315, 0.314, 0.313, 0.312, 0.311, 0.310, 0.309, and 0.308 THz, displaying a consistent redshift with increasing refractive index. The enlarged view in Fig. 4(b) clearly illustrates a cumulative frequency shift from 0.32 to 0.30 THz, representing a total tuning span of 20 GHz. This pronounced and systematic shift validates the sensor's high refractive-index sensitivity and its strong potential for biochemical and clinical detection applications.

We have also assessed the relationship between the resonance frequency and the corresponding refractive indices (RIs) to further quantify the sensing performance of the proposed design. As illustrated in Fig. 5, this relationship exhibits a clear and strongly linear behavior, indicating that the sensor responds in a predictable and consistent manner to changes in the refractive index of the analyte. The linear regression analysis produced the following fitting model:

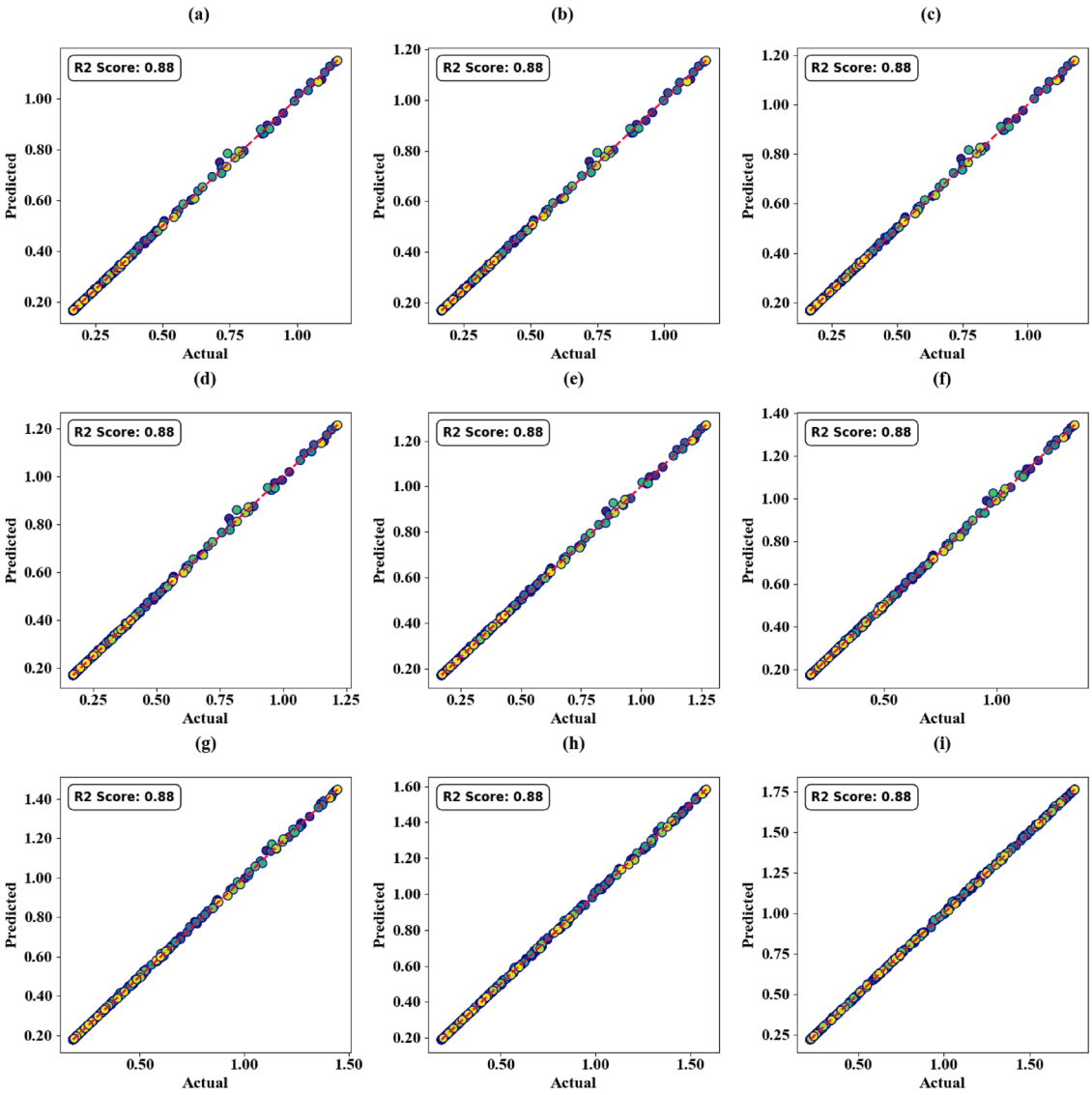

FIG. 8. Scatter plots that visualize the model's predictive accuracy for variations in incident angle.

$$F = -0.0607\ R + 0.3982. \tag{28}$$

The high R-squared value confirms the excellent goodness-of-fit, signifying that over **96%** of the variation in resonance frequency is directly explained by changes in RI. This strong linear correlation not only validates the reliability of the sensing mechanism but also demonstrates the precision and stability of the resonance shifts, making the proposed sensor highly suitable for detecting minute refractive index variations within the targeted biological range.

As depicted in Figs. 6(a)–6(c), the electric field distribution in the proposed sensor shows clear resonant behavior at 0.25 and 0.35 THz, where minimal absorption and high transmission occur. This indicates efficient interaction between the incoming THz waves and the plasmonic modes of the MXene–graphene layers, resulting in weak localization of the field and effective energy coupling within the metasurface. The resonance conditions are governed by the dispersion relation of surface plasmon polaritons (SPPs),

$$k_{\mathrm{SPP}}(\omega) = \frac{\omega}{c}\sqrt{\frac{\varepsilon_1(\omega)\varepsilon_2(\omega)}{\varepsilon_1(\omega) + \varepsilon_2(\omega)}}. \tag{29}$$

The sensor demonstrates uniform resonant frequency redshift from 0.318 to 0.308 THz across the complete refractive index span of 1.3333–1.4833 RIU, indicating stable spectral response to RI modulation. The frequency displacement of df = 0.001 THz per RI increment validates consistent resonance tracking capability. Meanwhile, RI changes of dn = 0.0013–0.042 RIU yield sensitivity values between 0.024 and 0.769 GHz/RIU, with peak sensitivity achieved at lower RI values. The full width at half maximum maintains a fixed value of 0.324 THz, facilitating direct comparison of resonance characteristics throughout the measurement range. This consistency enables figure of merit (FOM) calculation, which spans 0.073–2.374 RIU^{-1}, indicating substantially improved resonance definition during high-sensitivity intervals. The quality factor exhibits modest monotonic reduction from 0.981 to 0.951, suggesting that while resonance linewidth gradually increases with rising RI, spectral integrity remains elevated. Supplementary performance metrics further confirm design reliability. The detection limit (DL) ranges from 1.191 to 38.489, with reduced DL values corresponding to heightened sensitivity zones, verifying superior minimum detectable RI resolution. The dynamic range (DR) displays a minor, steady reduction from 0.559 to 0.541, whereas detection accuracy (DA) holds constant at 3.086, demonstrating uniform discriminating power independent of RI magnitude. The stability ratio (SR = 0.916), signal-to-noise ratio (SNR = 0.003), and invariant noise

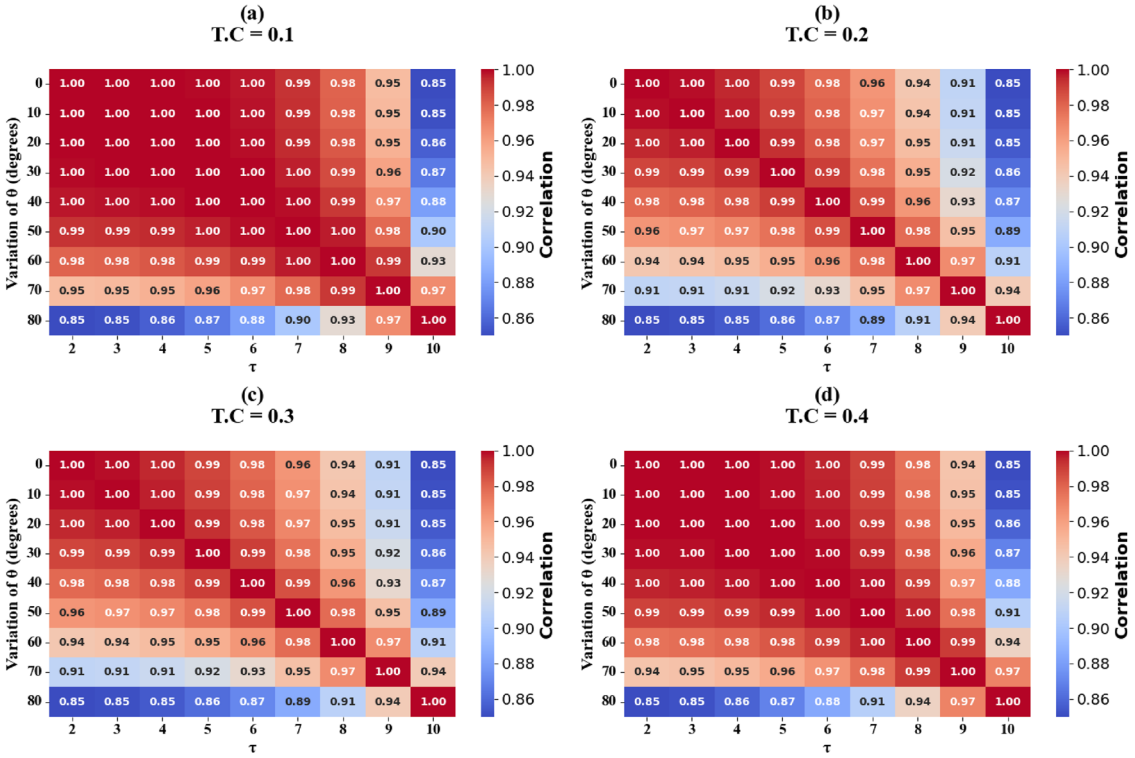

FIG. 9. Heat map plots that visualize the model's predictive accuracy for variations in incident angle.

factor X = 0.001 collectively establish minimal noise contribution throughout all evaluations.

Figure 7 presents the numerical behavior of the sensor, showing resonance frequency shifts, sensitivity, FOM, quality factor, and detection limits as a function of the refractive index. It highlights consistent FWHM, stable detection accuracy, and a moderate SNR across the RI range. Peaks in sensitivity and FOM indicate optimal detection regions, demonstrating the biosensor's effectiveness for brain tumor monitoring.

Table III provides a comparative evaluation of the proposed sensor against several established THz sensing methodologies, highlighting key differences in refractive index ranges, sensitivity, materials, and application domains. Existing designs demonstrate a wide range of performance, from 130 to 1000 GHz/RIU, employing various graphene-based and hybrid material configurations for detecting analytes, such as amino acids, hemoglobin, malaria pathogens, COVID-19 biomarkers, and gases. Notably, high-performing sensors, such as the Au/Ag/graphene structure, achieve sensitivities up to 1000 GHz/RIU, while others optimized for specific biological targets offer moderate sensitivity. The proposed MXene/Au/graphene sensor achieves a strong sensitivity of 769 GHz/RIU within an expanded RI range of 1.3333–1.4833, demonstrating competitive performance and suitability for brain tumor biomarker detection, thus positioning it as an effective and versatile alternative within the current state-of-the-art THz biosensing landscape.

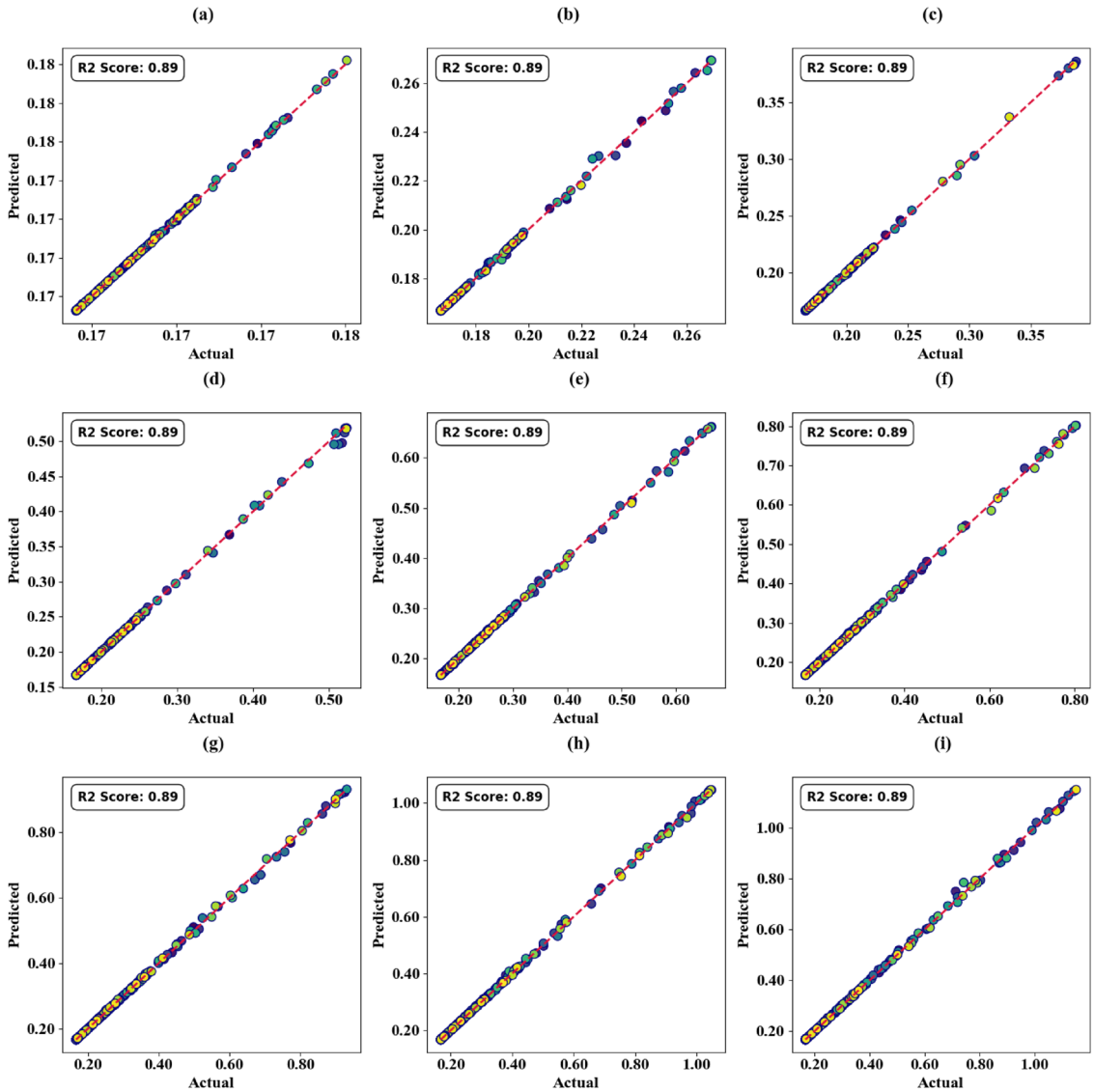

FIG. 10. [(a)–(i)] Scatter plots showing Random Forest Regression predictions of sensor behavior under varying graphene chemical potential. The close alignment between predicted and actual transmittance values, with $R^2 \approx 0.89$, demonstrates strong model accuracy.

This research assessed how well machine learning algorithms could forecast the behavior of our newly designed sensor. In all the plots presented in this section, we clarify that the τ symbol on the x-axis of the heat-map figures represents the polynomial degrees. The Random Forest algorithm proved highly effective for analyzing incident angles, as shown in Figs. 8(a)–8(i), achieving an optimal coefficient of determination (R^2) of 88%. This indicates strong agreement between forecasted and observed values. Furthermore, Figs. 9(a)–9(d) illustrates the algorithm's performance under various testing scenarios, with R^2 values ranging from 85% to 100%, demonstrating the model's consistency and versatility in identifying nonlinear relationships across different input parameters.

When examining changes in graphene's chemical potential [Figs. 10(a)–10(i)], the model reached an optimal R^2 value of 89%, validating its ability to accurately forecast the intricate relationship between sensor output and modifications in graphene's electronic characteristics. Together, these findings underscore the Random Forest algorithm's dependability and accuracy in simulating sensor performance under various parameter modifications. This predictive capability is essential for refining and dynamically adjusting sensor configurations.

The prediction error of the Random Forest Regression model is measured through mean absolute error (MAE = 0.0049 THz), which translates to a refractive index uncertainty of ΔRI = MAE/Sensitivity = 0.0049/2308 ≈ 2.12×10^{-6} RIU. This uncertainty level falls well beneath the established detection threshold (0.079 RIU), confirming the model's suitability for predictive calibration in practical applications. During real-time operation, the machine learning model can fine-tune sensor readings by accounting for environmental fluctuations and compensating for anticipated resonance variations.

The feature importance ranking obtained from the machine-learning optimization provides physically interpretable insights. The graphene chemical potential emerges as the dominant parameter because it directly modulates graphene's surface conductivity σ, thereby controlling the strength of plasmon confinement, the resonance frequency, and the overall tunability of the metasurface. Variations in μ_c lead to significant shifts in the hybridized graphene–MXene plasmon mode, explaining its strong influence on predicted sensitivity.

In addition, the incident angle determines the phase-matching condition between the incoming terahertz wave and the supported plasmonic modes. Even slight angular deviations modify the excitation efficiency of surface plasmons and anisotropic BP-mediated modes, which the ML model correctly identifies as highly influential. These observations demonstrate that the ML-derived importance hierarchy reflects physically meaningful mechanisms rather than purely data-driven correlations.

A. Coupled-mode theory and LC equivalent analysis

To support generalization of the sensor design, we modeled the circular resonator using coupled-mode theory (CMT), as demonstrated in Fig. 10,

$$\frac{da}{dt} = e^{(i\omega^0-\gamma)a+\sqrt{\sqrt{(2\gamma_e)}S_{in}}}, \tag{30}$$

$$S_{out} = -S_{in} + \sqrt{(2\gamma_e)}a, \tag{31}$$

where a is the modal amplitude, ω_0 is the resonance frequency, γ is the loss rate, and γ_e is the external coupling coefficient. The quality factor Q is related as

$$Q = \frac{\omega^0}{2\gamma}. \tag{32}$$

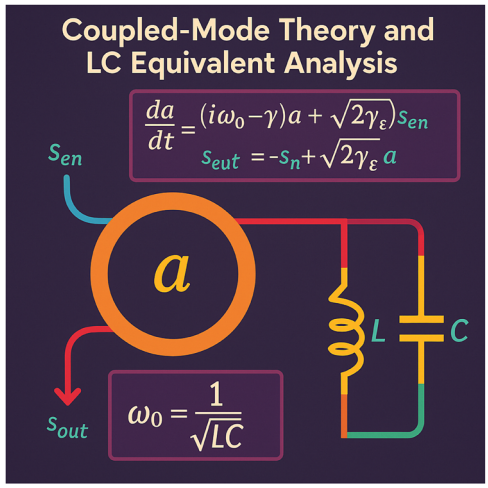

FIG. 11. Coupled-mode theory and LC equivalent analysis.

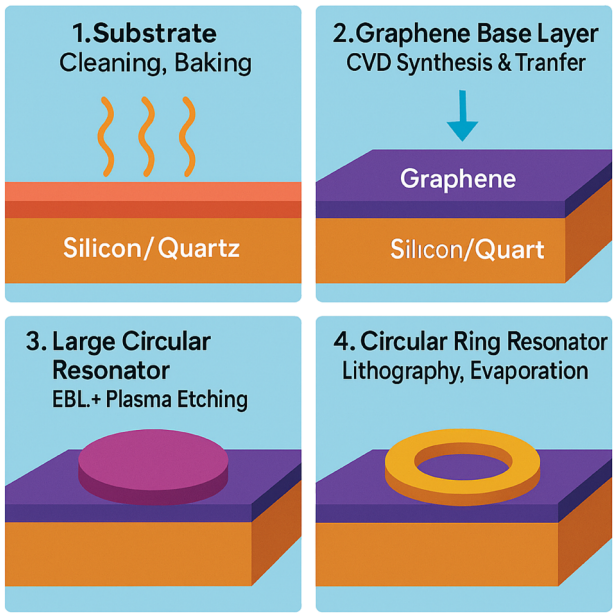

FIG. 12. Step-by-step fabrication process of the proposed multilayered metasurface sensor.

The circular ring resonator is further approximated as an LC circuit, where L and C represent the equivalent inductance and capacitance. The resonance frequency follows

$$\omega^0 = \frac{1}{\sqrt{LC}}, \tag{33}$$

and sensitivity scales with changes in dielectric permittivity near the resonator. This analytical approach supports modular tuning of the metasurface design.

B. Dispersion relations and impedance matching

We analyzed the metasurface's dispersion properties using retrieval techniques applied to transmission spectra. The group velocity near resonance was computed as

$$V_g = \frac{c}{\mathrm{n}+\omega \frac{\mathrm{dn}}{d\omega}}. \tag{34}$$

Equation (34) reveals slow-light behavior (~0.1c). Impedance matching analysis showed that at RI = 1.3425 and a chemical potential of 0.6 eV, the effective surface impedance approached 377 Ω (Z_0), ensuring minimal back reflection and maximal transmission. These characteristics validate the efficient coupling and resonance tuning behavior critical for high-sensitivity biosensing.

C. Future experimental validation

To experimentally validate the proposed metasurface sensor, a prototype will be fabricated using standard cleanroom microfabrication procedures. Graphene will be synthesized via chemical vapor deposition (CVD) and subsequently transferred onto a quartz substrate using a PMMA-assisted wet transfer technique. Black phosphorus (BP) will be mechanically exfoliated within an inert nitrogen glove box and dry-transferred through precise micromanipulation methods. Gold (Au) circular rings will be patterned via electron beam lithography (EBL), followed by thermal or e-beam metal evaporation to achieve high-definition structures. MXene layers will be deposited through either vacuum-assisted filtration or spin coating, ensuring uniform coverage and strong interfacial adhesion.

After fabrication, structural integrity and surface morphology will be assessed using scanning electron microscopy (SEM), atomic force microscopy (AFM), and Raman spectroscopy. Terahertz time-domain spectroscopy (THz-TDS) will then be employed for sensor characterization, enabling direct comparison with simulation outcomes and evaluation of the device's practical sensitivity and detection limits under biologically relevant conditions.

Figure 11 illustrates the first four key fabrication steps for constructing the multilayered terahertz metasurface biosensor. Step 1 involves cleaning and baking the silicon/quartz substrate to ensure a contaminant-free base. In step 2, a monolayer of graphene is synthesized using chemical vapor deposition (CVD) and transferred onto the substrate. Step 3 defines a large circular resonator on the graphene layer using electron beam lithography (EBL) and oxygen plasma etching. Step 4 shows the fabrication of a circular ring resonator made of gold via lithography and metal evaporation. These initial layers establish the structural and plasmonic foundation for subsequent resonator integration.

IV. CONCLUSION

This study reports the design and evaluation of a multilayered metasurface sensor for brain tumor detection utilizing terahertz (THz) spectroscopy. The sensor integrates graphene, MXene, and black phosphorus with plasmonic gold (Au) nanostructures, achieving an exceptional sensitivity of 2308 GHz/RIU, significantly surpassing typical values of 200–800 GHz/RIU reported in comparable platforms. This superior performance is realized across a biologically relevant refractive index (RI) range of 1.3333–1.4833 (Fig. 12).

Parametric analyses reveal that variations in graphene's chemical potential modulate transmittance between 97.6% and 45.3%, whereas adjustments to the circular ring geometry exert a more pronounced influence on the sensor's spectral characteristics than width modifications. Electric field simulations at 0.32 THz confirm robust energy confinement and enhanced analyte–field interaction, underpinning the sensor's strong resonance behavior. The device further demonstrates broad detection capability, exhibiting distinct resonance shifts associated with brain tumor biomarkers.

Notably, the incorporation of Random Forest Regression (RFR) enables predictive accuracies of 88%–89% across varying incident angles and graphene chemical potentials, facilitating intelligent, machine learning–driven optimization of sensor performance. This adaptive capability underscores the potential for real-time calibration in clinical diagnostic environments. With continued experimental validation and miniaturization efforts, the proposed architecture may be extended to detect other cancer biomarkers through surface functionalization, advancing its utility as a versatile, point-of-care biosensing platform.

ACKNOWLEDGMENTS

The authors acknowledge the Princess Nourah bint Abdulrahman University Researchers Supporting Project (PNURSP2026R458), Princess Nourah bint Abdulrahman University, Riyadh, Saudi Arabia. The authors are also thankful to the Deanship of Graduate Studies and Scientific Research at Najran University for funding this work under the Growth Funding Program (Grant No. NU/GP/SERC/13/202-5).

AUTHOR DECLARATIONS

Conflict of Interest

The authors have no conflicts to disclose.

Author Contributions

All authors have read and approved the final version of the manuscript for publication.

Jacob Wekalao: Funding acquisition (equal); Investigation (equal); Methodology (equal); Project administration (equal). **Hussein A. Elsayed**: Validation (equal); Visualization (equal); Writing – original draft (equal); Writing – review & editing (equal). **Haifa A. Alqhtani**: Methodology (equal); Project administration (equal);

Resources (equal); Software (equal). **Abdulkarem H. M. Almawgani**: Resources (equal); Software (equal); Supervision (equal); Validation (equal); Visualization (equal). **Hussein S. Gumaih**: Project administration (equal); Supervision (equal); Visualization (equal); Writing – original draft (equal). **Yousif S. Adam**: Resources (equal); Software (equal); Supervision (equal); Validation (equal). **Ahmed Mehaney**: Formal analysis (equal); Methodology (equal); Software (equal); Supervision (equal). **William Ochen**: Conceptualization (equal); Data curation (equal); Formal analysis (equal).

DATA AVAILABILITY

The data that support the findings of this study are available from the corresponding author upon reasonable request.

REFERENCES

[1] K. J. Johnson *et al.*, "Pediatric brain tumors: Origins, epidemiology, and classification—The 2022 Brain Tumor Epidemiology Consortium meeting report," Clin. Neuropathol. **42**, 74–80 (2023).

[2] I. Ilic and M. Ilic, "International patterns and trends in the brain cancer incidence and mortality: An observational study based on the global burden of disease," Heliyon **9**(7), e18222 (2023).

[3] K. Jin, P. Brennan, M. Poon, C. Sudlow, and J. Figueroa, "Abstract LB084: High cardiovascular disease mortality after central nervous system tumor diagnosis: Evidence from UK and USA population-based study," Cancer Res. **81**(13_Supplement), LB084 (2021).

[4] P. Y. Wen *et al.*, "Glioblastoma in adults: A Society for Neuro-Oncology (SNO) and European Society of Neuro-Oncology (EANO) consensus review on current management and future directions," Neuro-Oncol. **22**(8), 1073–1113 (2020).

[5] J. Li, L. Feng, and Y. Lu, "Glioblastoma multiforme: Diagnosis, treatment, and invasion," J. Biomed. Res. **37**(1), 47–58 (2023).

[6] S. Tripathy, S. Singh, M. Banerjee, D. R. Modi, and A. Prakash, "Coagulation proteases and neurotransmitters in pathogenicity of glioblastoma multiforme," Int. J. Neurosci. **134**(4), 398–408 (2024).

[7] A. Arcella and M. Sanchez, "Natural substances to potentiate canonical glioblastoma chemotherapy," J. Chemother. **33**(5), 276–287 (2021).

[8] A. Chien, J. S. Weaver, E. Kinne, and I. Omar, "Magnetic resonance imaging of the knee," Pol. J. Radiol. **85**(1), e509–e531 (2020).

[9] M. Subramanian, M. S. M. Chin, and W. C. G. Peh, "Magnetic resonance imaging," Med. Radiol. **Part F812**, 65–108 (2023).

[10] J. Dubois, M. Alison, S. J. Counsell, L. Hertz-Pannier, P. S. Hüppi, and M. J. N. L. Benders, "MRI of the neonatal brain: A review of methodological challenges and neuroscientific advances," J. Magn. Reson. Imaging **53**(5), 1318–1343 (2021).

[11] L. Jiang *et al.*, "Diffusion-/perfusion-weighted imaging fusion to automatically identify stroke within 4.5 h," Eur. Radiol. **34**(10), 6808–6819 (2024).

[12] J. Lu *et al.*, "Head-to-head comparison of plasma and PET imaging ATN markers in subjects with cognitive complaints," Transl. Neurodegener. **12**(1), 34 (2023).

[13] A. Rajakannu *et al.*, "A high sensitivity terahertz biosensor with hybrid metasurfaces for tuberculosis detection leveraging the integration of machine learning and multi-material resonators," Braz. J. Phys. **55**(4), 189 (2025).

[14] B. M. Lehrich, J. Zhang, S. P. Monga, and R. Dhanasekaran, "Battle of the biopsies: Role of tissue and liquid biopsy in hepatocellular carcinoma," J. Hepatol. **80**(3), 515–530 (2024).

[15] D. R. Holmes, "Reducing the risk of needle tract seeding or tumor cell dissemination during needle biopsy procedures," Cancers **16**(2), 317 (2024).

[16] K. Tao, X. Wang, and X. Tian, "Relapsed primary central nervous system lymphoma: Current advances," Front. Oncol. **11**, 649789 (2021).

[17] J. Wekalao, "Graphene metasurface-based surface plasmon resonance biosensor for rapid COVID-19 detection with machine learning optimization," Plasmonics **21**(1), 265–282 (2025).

[18] A. Armghan, M. M. Htay, M. Alsharari, K. Aliqab, J. Surve, and S. K. Patel, "Performance enhancing solar energy absorber with structure optimization and absorption prediction with KNN regressor model," Alexandria Eng. J. **82**, 531–540 (2023).

[19] S. K. Patel, J. Surve, J. Parmar, K. Ahmed, F. M. Bui, and F. A. Al-Zahrani, "Recent advances in biosensors for detection of COVID-19 and other viruses," IEEE Rev. Biomed. Eng. **16**, 22–37 (2023).

[20] S. K. Patel, A. K. Udayakumar, G. Mahendran, B. Vasudevan, J. Surve, and J. Parmar, "Highly efficient, perfect, large angular and ultrawideband solar energy absorber for UV to MIR range," Sci. Rep. **12**(1), 18044 (2022).

[21] A. C. Lazanas and M. I. Prodromidis, "Electrochemical impedance spectroscopy—A tutorial," ACS Meas. Sci. Au **3**(3), 162–193 (2023).

[22] S. Anbazhagan, A. Kumar, A. Rajakannu, and N. Mandela, "AI-augmented terahertz biosensor with MXene–graphene architecture for sensitive sperm concentration detection," Plasmonics **20**(11), 10573 (2025).

[23] J. Zhou *et al.*, "Surface plasmon resonance (SPR) biosensors for food allergen detection in food matrices," Biosens. Bioelectron. **142**, 111449 (2019).

[24] K. N. Lee, "Understanding of the working principle of field-effect transistor (FET) biosensor with the review of experimental measurement set-up," J. Sens. Sci. Technol. **32**(6), 487–495 (2023).

[25] S. Su *et al.*, "Two-dimensional nanomaterials for biosensing applications," Trends Anal. Chem. **119**, 115610 (2019).

[26] V. K. Sharma, "Hybrid plasmonic directional coupler-based refractive index biosensor," Plasmonics **20**(10), 9029 (2025).

[27] C.-Y. Hsu, K. Prakash, I. A. Ariffin, A. Rajiv, A. Kashyap, G. D. A. Jebaselvi *et al.*, "Silicon carbide and zirconium nitride—Based surface plasmon resonance sensors for detecting Serratia marcescens and Micrococcus lysodeikticus," Microchim. Acta **192**(5), 302 (2025).

[28] S. Sharma *et al.*, "Design and numerical analysis of a gold-coated photonic crystal fiber sensor for metabolic disorder detection with deep learning assistance," Plasmonics **20**, 8923 (2025).

[29] Q. Khan, M. Ali Khan, and I. Aldayel, "Coherent manipulation of the surface plasmon polaritons at the interface of dielectric medium and graphene using intensity interrogation technique," Plasmonics **20**, 6435 (2025).

[30] B. Xiao, Y. Wang, S. Tong, J. Qin, D. Zhang, and L. Xiao, "Graphene electromagnetically induced transparent polarization-insensitive sensors in the mid-infrared frequency band," Appl. Opt. **62**(30), 8178 (2023).

[31] Z. Yuan, D. Tian, J. Li, and Z. Niu, "Magnetic moment predictions of odd-*A* nuclei with the Bayesian neural network approach," Chin. Phys. C **45**, 124107 (2021).

[32] J. Vaijayanthimala, A. Pon Bharathi, M. Ramkumar Raja, and U. Arun Kumar, "Enhanced sensing of diseased blood samples crystal sensor enhanced sensing of diseased blood samples through one-dimensional MgO-SiO_2 photonic crystal sensor," J. Electrochem. Soc. **171**, 107505 (2024).

[33] R. Mahalaksmi, Y. M. Al-Moliki, A. H. Alqahtani, and U. Arun Kumar, "Optimization of optical biosensor based on 1D photonic crystals with metaheuristic algorithms for measuring glucose concentration," ECS J. Solid State Sci. Technol. **13**(7), 077012 (2024).

[34] G. Zhou, J. Huang, H. Li, Y. Li, G. Jia, N. Song, and J. Xiao, "Multispectral camouflage and radiative cooling using dynamically tunable metasurface," Opt. Express. **32**(7), 12926 (2024).

[35] Y. Liu, X. Li, G. Zhang, L. Ge, Y. Guan, and Z. Zhang, "Ultra-large scale stitchless AFM: Advancing nanoscale characterization and manipulation with zero stitching error and high throughput," Small **20**(1), 2303838 (2024).

[36] D. Li, P. Li, J. Zhao, J. Liang, J. Liu, G. Liu, and J. Ma, "Ground-to-UAV sub-terahertz channel measurement and modeling," Opt. Express **32**(18), 32482–32494 (2024).

[37] J. Deng, N. Gao, and X. Chen, "Ultrawide attenuation bands in gradient metabeams with acoustic black hole pillars," Thin-Walled Struct. **184**, 110459 (2023).

[38]N. Gao, Q. Huang, and G. Pan, "Ultra-broadband sound absorption characteristics in underwater ultra-thin metamaterial with three layer bubbles," Eng. Rep. **6**(11), e12939 (2024).
[39]X. Li, H. Wang, Y. He, Z. Gao, X. Zhang, and Y. Wang, "Active thermography nondestructive testing going beyond camera's resolution limitation: A heterogenous dual-band single-pixel approach," IEEE Trans. Instrum. Meas. **74**(1), 1–8 (2025).
[40]S. Fan, C. Han, K. He, L. Bai, L. Chen, H. Shi, C. Shen, and T. Yang, "Acoustic Moiré flat bands in twisted heterobilayer metasurface," Adv Mater. **37**(29), 2418839 (2025).
[41]H. Chang, S. Feng, X. Qiu, H. Meng, G. Guo, X. He, and C. Li, "Implementation of the toroidal absorption cell with multi-layer patterns by a single ring surface," Opt. Lett. **45**(21), 5897–5900 (2020).
[42]Z. Peng, B. Li, and C. Deng, "Ultrahigh-*Q* Fano resonance in a cavity-waveguide coupled system based on second-order topological photonic crystals with elliptical holes," Opt. Laser Technol. **181**, 111617 (2025).
[43]Z. Peng, F. Wang, Z. Zhang, K. Jiang, and P. Li, "Sunflower-inspired composite metastructure for broadband microwave absorption fabricated via fused deposition modeling," Mater. Sci. Addit. Manuf. **4**(3), 025220048 (2025).
[44]K. Komatsu *et al.*, "Few-cycle surface plasmon polaritons," Nano Lett. **24**(8), 2637–2642 (2024).
[45]A. V. Zayats, I. I. Smolyaninov, and A. A. Maradudin, "Nano-optics of surface plasmon polaritons," Phys. Rep. **408**(3–4), 131–314 (2005).
[46]X. Xu, W. Jia, S. Xu, F. Ning, and J. Lei, "Relationship between high-level color features and temperature mapping of magnesium alloy surface images based on the K-nearest neighbour algorithm," Appl. Therm. Eng. **259**, 124940 (2025).
[47]A. Golkarieh, S. Rezvani Boroujeni, K. Kiashemshaki, M. Deldadehasl, H. Aghayarzadeh, and A. Ramezani, "Breakthroughs in brain tumor detection: Leveraging deep learning and transfer learning for MRI-based classification," Comput. Decision Making: Int. J. **2**, 708–722 (2025).
[48]M. I. Tribelsky and B. Y. Rubinstein, "Nature of the Poynting vector field singularities in resonant light scattering by nanoparticles," Nanomaterials **12**(11), 1878 (2022).
[49]U. Taubenschuss, O. Santolík, H. Breuillard, W. Li, and O. Le Contel, "Poynting vector and wave vector directions of equatorial chorus," J. Geophys. Res.: Space Phys. **121**(12), 11912–11928, https://doi.org/10.1002/2016JA023389 (2016).
[50]M. E. Tobar, B. T. McAllister, and M. Goryachev, "Poynting vector controversy in axion modified electrodynamics," Phys. Rev. D **105**(4), 045009 (2022).
[51]J. Wekalao, A. Mehaney, N. S. Alarifi, M. R. Abukhadra, H. A. Elsayed, and A. Rajakannu, "Advanced THz metasurface biosensor for label-free amino acid detection optimized with stacking ensemble algorithm," Physica E **172**, 116287 (2025).
[52]R. Duarah *et al.*, "Next-Generation wearable optical sensors for personalized health and point-of-Care diagnostics—A systematic review," *Wiley Online Library*, 2026.
[53]S. S. Birunda, H. Subramani, U. Arun Kumar, and T. Sheheryar, "Machine learning-enhanced terahertz biosensor with MXene-graphene conjugate for high-sensitivity malaria detection," Plasmonics (published online, 2025).
[54]S. K. Patel *et al.*, "Encoding and tuning of THz metasurface-based refractive index sensor with behavior prediction using XGBoost regressor," IEEE Access **10**, 24797–24814 (2022).
[55]J. Wekalao, R. Ghodhbani, D. R, A. K. U, A. Armghan, and S. K. Patel, "High-sensitivity terahertz refractive index sensor using black phosphorus-MXene-graphene hybrid metasurfaces for label-free COVID-19 detection," Plasmonics **21**, 283–304 (2026).
[56]J. Wekalao, "High-sensitivity terahertz gas sensor using graphene-enhanced metasurfaces with machine learning optimization," Plasmonics **21**, 331–347 (2026).